Mon. Not. R. Astron. Soc. **000**, 000–000 (0000) Printed 28 September 2007 (MN LATEX style file v2.2)

# Understanding the shape of the halo-mass and galaxy-mass cross-correlation functions

Eric Hayashi and Simon D.M. White
*Max Planck Institute for Astrophysics, Karl-Schwarzschild Strasse 1, D-85748 Garching, Germany*



28 September 2007

**ABSTRACT**
We use the Millennium Simulation to measure the cross-correlation between halo centres and mass (or equivalently the average density profiles of dark haloes) in a ΛCDM cosmology. We present results for radii in the range $10\ h^{-1}\mathrm{kpc} < r < 30\ h^{-1}\mathrm{Mpc}$ for halo masses in the range $4 \times 10^{10}\ h^{-1}\mathrm{M}_{\odot} < M_{200} < 4 \times 10^{14}\ h^{-1}\mathrm{M}_{\odot}$. Both at $z = 0$ and at $z = 0.76$ these cross-correlations are surprisingly well fit by approximating the inner region by a density profile of NFW or Einasto form, the outer region by a biased version of the linear mass autocorrelation function, and by adopting the maximum of the two where they are comparable. We use a simulation of the formation of galaxies within the Millennium Simulation to explore how these results are reflected in cross-correlations between galaxies and mass. These are directly observable through galaxy-galaxy lensing. Here also we find that simple models can represent the simulation results remarkably well, typically to $\lesssim 10\%$. Such models can be used to extend our results to other redshifts, to cosmologies with other parameters, and to other assumptions about how galaxies populate dark haloes. The characteristic features predicted in the galaxy-galaxy lensing signal should provide a strong test of the ΛCDM cosmology as well as a route to understanding how galaxies form within it.

**Key words:** cosmology: theory – dark matter – large-scale structure of the universe

## 1 INTRODUCTION

Weak gravitational lensing has opened a new window onto the large scale distribution of matter. Gravitational lensing by foreground mass induces correlated distortions, or shear, in the observed shapes of distant galaxies. In galaxy-galaxy lensing, the signal from many galaxies is added together in order to measure the average (projected) distribution of mass around galaxies. This can be interpreted as the mass in the extended dark matter halos which surround galaxies, or, more generally, as the cross-correlation between lens galaxies and the projected mass distribution. Several groups have successfully applied this technique to large imaging surveys to derive constraints on the mass associated with galaxies as a function of galaxy properties such as luminosity and morphology (Brainerd et al. 1996; dell'Antonio and Tyson 1996; Griffiths et al. 1996; Hudson et al. 1998; Fischer et al. 2000; McKay et al. 2001; Hoekstra et al. 2003; Sheldon et al. 2004).

Theoretical predictions for cross-correlations between galaxies and mass, $\xi_{\mathrm{gm}}$, have made use both of numerical simulations (Guzik and Seljak 2001; Yang et al. 2003; Tasitsiomi et al. 2004; Weinberg et al. 2004) and of analytic halo models (Seljak 2000; Guzik and Seljak 2002). Tasitsiomi et al. (2004) show that the amplitude and shape of $\xi_{\mathrm{gm}}$ predicted by cosmological simulations, when combined with a simple model for populating halos with galaxies, are in good agreement with observational results based on Sloan Digital Sky Survey (SDSS) data (Sheldon et al. 2004). Mandelbaum et al. (2005) also find that these simulation results can be accurately reproduced by the halo model of Seljak (2000) and Guzik and Seljak (2002).

In this work we calculate the cross-correlation between halos and mass, $\xi_{\mathrm{hm}}$, and between galaxies and mass, $\xi_{\mathrm{gm}}$, in the Millennium Simulation, a very large, high-resolution simulation of a ΛCDM cosmology. We also present simple models for $\xi_{\mathrm{hm}}$ and $\xi_{\mathrm{gm}}$ which can be used to interpret the shapes of these functions and to extend our results to other redshifts, cosmologies and halo population models.

The organization of this paper is as follows. In §2 we describe the Millennium Simulation and the halo and

galaxy catalogues used in this study. In §3 we show $\xi_{\rm hm}$ calculated for halo samples with a range of masses and we present a model which accurately reproduces these results. In §4 we show $\xi_{\rm gm}$ for both central and satellite galaxies as a function of their luminosity, and we present models for each of these and for the combined galaxy sample. Finally, we summarize our results in §5.

## 2 SIMULATIONS

This study makes use of the Millennium Simulation[1] (Springel et al. 2005), a large cosmological N-body simulation carried out by the Virgo Consortium[2]. In this simulation a flat ΛCDM cosmology is adopted, with $\Omega_{\rm dm} = 0.205$, $\Omega_{\rm b} = 0.045$ for the current densities in cold dark matter and baryons, $h = 0.73$ for the present dimensionless value of the Hubble constant, $\sigma_8 = 0.9$ for the *rms* linear mass fluctuation in a sphere of radius $8\ h^{-1}$Mpc extrapolated to $z = 0$, and $n = 1$ for the slope of the primordial fluctuation spectrum. The simulation follows $2160^3$ dark matter particles from $z = 127$ to $z = 0$ within a periodic cube $L_{\rm box} = 500\ h^{-1}$Mpc on a side. The individual particle mass is thus $8.6 \times 10^8\ h^{-1}M_\odot$, and the gravitational force is softened with a Plummer-equivalent comoving softening of $5\ h^{-1}$kpc. Initial conditions were generated using the Boltzmann code CMBFAST (Seljak and Zaldarriaga 1996) to generate a realization of the desired power spectrum which was then imposed on a glass-like uniform particle load (White 1996). A modified version of the TREE-PM N-body code GADGET2 (Springel et al. 2001b, 2005) was used to carry out the simulation and full particle data are stored at 64 output times approximately equally spaced in the logarithm of the expansion factor at early times and at roughly 300 Myr intervals after $z = 2$.

In each output of the simulation, halos are identified using a friends-of-friends (FoF) groupfinder with a linking length of $b = 0.2$ (Davis et al. 1985). Each FoF halo is decomposed into a collection of locally overdense, self-bound substructures (or subhalos) using the SUBFIND algorithm of Springel et al. (2001a). Of these subhalos, one is typically much larger than the others and contains most of the mass of the halo. We identify this as the main subhalo and define its centre as the position of the particle with the minimum potential. The virial radius, $r_{200}$, is defined as the radius of a sphere that encompasses a mean density 200 times the critical value, and the virial mass, $M_{200}$, is the mass within this radius.

Semi-analytic techniques have been used to simulate the evolution of the galaxy population within the Millennium Simulation, as described by Springel et al. (2005) and Croton et al. (2006). In this approach the evolution of the baryonic component is followed using a set of simple prescriptions for gas cooling, star formation, supernova and AGN feedback, chemical enrichment, galaxy merging and other relevant physical processes. These models can be applied repeatedly to the stored histories of the dark matter halos and subhalos with different parameter choices for the model, or indeed with different physical assumptions in the modelling. In this work we use the semi-analytic galaxy catalogue described in detail in Croton et al. (2006). We note that various aspects of the clustering properties of halos and galaxies in the Millennium Simulation have been investigated in Springel et al. (2005), Gao et al. (2005), Harker et al. (2006),Wang et al. (2006), Springel et al. (2006), Croton et al. (2006), Li et al. (2006), Croton et al. (2007) and Gao and White (2007). Studies of halo density profiles in the simulation have been carried out by Neto et al. (2007) and Gao and White (2007).

[1] http://www.mpa-garching.mpg.de/millennium/
[2] http://www.virgo.dur.ac.uk/

## 3 HALO-MASS CROSS-CORRELATIONS

Given a density field, $\rho(\mathbf{x})$, the density fluctuation field is defined as

$$\delta(\mathbf{x}) = \frac{\rho(\mathbf{x}) - \overline{\rho}}{\overline{\rho}}. \quad (1)$$

The two-point autocorrelation function is defined as

$$\xi(\mathbf{r}) \equiv \langle \delta(\mathbf{x})\delta(\mathbf{x}+\mathbf{r})\rangle. \quad (2)$$

Assuming isotropy reduces this to a function of the separation, $\xi(r)$. This is interpreted as a measurement of the excess probability above random of finding a pair of objects with separation $r$ (Peebles 1980). In the case of two different populations of objects, $\delta_{\rm a}(\mathbf{x})$ and $\delta_{\rm b}(\mathbf{x})$, the two-point cross-correlation function is given by

$$\xi_{\rm ab}(\mathbf{r}) \equiv \langle \delta_{\rm a}(\mathbf{x})\delta_{\rm b}(\mathbf{x}+\mathbf{r})\rangle. \quad (3)$$

If we consider the cross-correlation between halo centres and mass, the cross-correlation function $\xi_{\rm hm}(r)$ simply reflects the spherically-averaged halo density profile averaged over all halos in the sample. This can be seen by combining eqs. 1 and 3 to give

$$\xi_{\rm hm}(r) = \frac{\langle\rho(r)\rangle - \overline{\rho}_{\rm m}}{\overline{\rho}_{\rm m}}, \quad (4)$$

where $r$ is the radial distance from the halo centre and $\overline{\rho}_{\rm m} = \rho_{\rm crit}\Omega_{\rm m}$ is the mean density of the Universe.

Figure 1 shows halo-mass cross-correlations along with the mass autocorrelation function for the Millennium Simulation. The halo-mass cross-correlations are computed using the centres of the main subhalos of all FoF halos with mass $M_{200} \geq 4 \times 10^{10}\ h^{-1}M_\odot$, corresponding to $\gtrsim 50$ particles. Seven halo samples are shown, each spanning a factor of two in mass. The number of halos in each sample is listed in Table 1. We have computed cross-correlations also for the mass ranges not included in this plot and table, and we have checked that they also fit the models we discuss below. However, for clarity we refrain from showing them or discussing them further.

The shape of the halo-mass cross-correlation is clearly defined by two parts, commonly referred to as the one-halo and two-halo terms since they are dominated by particles within the same halo and in different halos, respectively. Figure 1 shows that on large scales

**Table 1.** Properties of halo samples taken from the Millennium Simulation.

| Mass range $[h^{-1}M_\odot]$ | $N_{\rm halos}$ | $< M_{200} >$ $[h^{-1}M_\odot]$ | $< R_{200} >$ $h^{-1}$Mpc | Fit $M_{200}$ $[h^{-1}M_\odot]$ | Fit $R_{200}$ $h^{-1}$Mpc | Fit $c_{200}$ | $r_{\rm trans}$ $h^{-1}$Mpc |
|---|---|---|---|---|---|---|---|
| $[4.0, 8.0] \times 10^{10}$ | 2491565 | $5.59 \times 10^{10}$ | 0.062 | $5.66 \times 10^{10}$ | 0.062 | 9.8 | 0.11 |
| $[1.6, 3.2] \times 10^{11}$ | 774837 | $2.23 \times 10^{11}$ | 0.098 | $2.26 \times 10^{11}$ | 0.099 | 9.1 | 0.19 |
| $[6.4, 12.8] \times 10^{11}]$ | 230429 | $8.92 \times 10^{11}$ | 0.16 | $9.05 \times 10^{11}$ | 0.16 | 8.3 | 0.33 |
| $[2.56, 5.12] \times 10^{12}$ | 67400 | $3.56 \times 10^{12}$ | 0.25 | $3.62 \times 10^{12}$ | 0.25 | 7.5 | 0.74 |
| $[1.02, 2.048] \times 10^{13}$ | 18322 | $1.42 \times 10^{13}$ | 0.39 | $1.45 \times 10^{13}$ | 0.40 | 6.7 | 1.28 |
| $[4.1, 8.192] \times 10^{13}$ | 4274 | $5.63 \times 10^{13}$ | 0.62 | $5.79 \times 10^{13}$ | 0.63 | 5.7 | 2.20 |
| $[1.64, 3.277] \times 10^{14}$ | 650 | $2.22 \times 10^{14}$ | 0.98 | $2.32 \times 10^{14}$ | 1.00 | 4.7 | 3.78 |

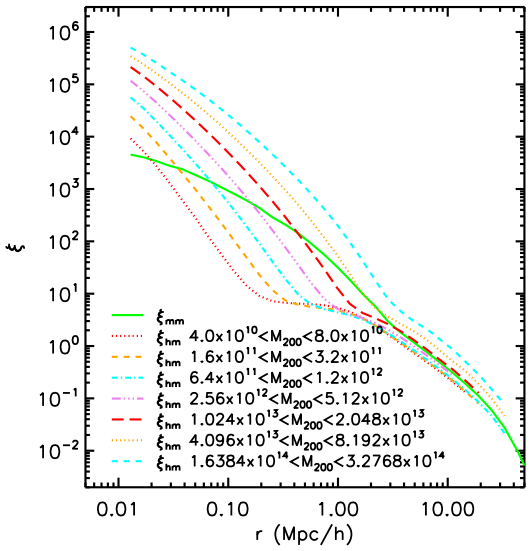


**Figure 1.** Cross-correlations between halo centres and the mass in the Millennium Simulation at $z = 0$. The solid curve shows the mass autocorrelation function, $\xi_{\rm mm}$ for comparison. On large scales, $r \gtrsim 3\ h^{-1}$Mpc, the cross-correlation functions follow the mass autocorrelation function with a constant bias factor. On small scales, $\xi_{\rm hm}(r)$ reflects the mean density profile of the individual halos. Note the sharp transition between the two regimes.

$\xi_{\rm hm}(r)$ follows closely the mass auto-correlation function, $\xi_{\rm mm}$, with a mass-dependent offset in amplitude known as the halo bias factor, $b(M)$. The transition between the two regimes is remarkably sharp and takes place at an overdensity of approximately seven times the mean density, i.e., $\xi_{\rm hm} \simeq 6$.

We construct a simple model for $\xi_{\rm hm}(r)$ as follows:

$$\xi_{\rm model}(r; M) = \begin{cases} \xi_{\rm 1h}(r) & \text{if } \xi_{\rm 1h}(r) \geq \xi_{\rm 2h}(r), \\ \xi_{\rm 2h}(r) & \text{if } \xi_{\rm 1h}(r) < \xi_{\rm 2h}(r), \end{cases} \quad (5)$$

$$\xi_{\rm 1h}(r) = \frac{\rho_{\rm halo}(r; M) - \overline{\rho}_{\rm m}}{\overline{\rho}_{\rm m}} \quad (6)$$

$$\xi_{\rm 2h}(r) = b(M)\xi_{\rm lin}(r), \quad (7)$$

where $\xi_{\rm lin}(r)$ is the mass autocorrelation function predicted by linear theory. The main ingredients of the model are the halo density profile, $\rho_{\rm halo}$, and the bias factor $b(M)$ which we now describe in detail.

### 3.1 The one-halo term

The density profiles of CDM halos have been studied extensively with high resolution N-body simulations over the past decade. Early results indicated that the density increases steeply towards the centres of halos (Frenk et al. 1985; Quinn et al. 1986; Dubinski and Carlberg 1991). Navarro et al. (1996, 1997, hereafter NFW) suggested the following simple fitting formula to describe the density profile of simulated halos:

$$\frac{\rho_{\rm NFW}(r)}{\rho_{\rm crit}} = \frac{\delta_0}{(r/r_s)(1 + r/r_s)^2}, \quad (8)$$

where $\rho_{\rm crit}$ is the critical density. Note that the slope of the NFW profile is shallower (steeper) than the isothermal profile inside (outside) the characteristic scale radius, $r_s$. Integrating this density profile out to the virial radius, $r_{200}$, gives the following relation for the dimensionless density parameter

$$\delta_0 = \frac{200}{3} \frac{c_{200}^3}{\ln(1 + c_{200}) - c_{200}/(1 + c_{200})} \quad (9)$$

where the concentration parameter $c_{200} = r_{200}/r_s$. Since the halo mass and virial radius are related through $M_{200} = 200\ \rho_{\rm crit}(4\pi/3)\ r_{200}^3$, the independent parameters in the NFW profile are effectively the halo mass and concentration. Furthermore, these properties are known to be correlated in simulated halos, in the sense that low-mass halos are more central concentrated than high-mass halos. This is generally interpreted in terms of the mean density of the universe at the time of formation of a halo. Since low-mass systems typically collapse at higher redshift, the characteristic density and concentration of such systems is larger with respect to high-mass systems. The concentration-mass relation has been studied extensively with cosmological simulations and several authors have proposed models for predicting the average value of $c_{200}$ as a function of halo mass and redshift (Navarro et al. 1997; Bullock et al. 2001; Eke et al. 2001; Macciò et al. 2007; Neto et al. 2007; Gao and White 2007). Adopting such a model therefore fully specifies the density profile of a typical halo of a given mass $M_{200}$ at a given redshift.

The most recent high resolution N-body simulations have revealed small but significant deviations from the NFW formula. Navarro et al. (2004, hereafter N04) show that the density profiles become shallower towards the halo centre more gradually than the NFW formula predicts, causing NFW fits to underestimate the density

in the inner regions. These authors propose an improved fitting formula with the following form:

$$\ln \frac{\rho_\alpha}{\rho_{-2}} = \frac{-2}{\alpha}\left[\left(\frac{r}{r_{-2}}\right)^\alpha - 1\right], \qquad (10)$$

where $\rho_{-2}$ and $r_{-2}$ are the density and radius at which the logarithmic slope of the density profile $\mathrm{d}\log\rho_\alpha/\mathrm{d}\log r = -2$, and the parameter $\alpha$, controls the rate of change of the logarithmic slope with radius. Higher values of $\alpha$ cause the profile to become shallower more quickly toward the centre of the halo. Unlike the NFW profile, eq. 10 does not converge to a power law at small radii, instead reaching a finite density at the centre. N04 found a relatively small range of values, $0.12 \leq \alpha \leq 0.22$, to fit the density profiles of simulated halos over a wide range in mass ($8\times10^9\ h^{-1}M_\odot \lesssim M_{200} \lesssim 8\times10^{14}\ h^{-1}M_\odot$). A spatial density profile of this form was first proposed in a different context by Einasto (1965) so we will hereafter refer to it as the Einasto profile. Prada et al. (2006) recently used the NFW and Einasto formulae to fit halo density profiles out to radii far beyond the virial radius. These authors find the mean density to give a significant contribution to the density profile at large distances, i.e., the halo profile is better fit by

$$\rho_{\rm halo}(r) = \rho_\alpha(r) + \overline{\rho}_{\rm m}. \qquad (11)$$

With this modification, the one-halo term becomes

$$\xi_{\rm 1h}(r) = \frac{\rho_\alpha(r)}{\overline{\rho}_{\rm m}}. \qquad (12)$$

In subsections 3.3 and 3.5 we investigate the accuracy of our model for $\xi_{\rm hm}$ using the NFW and Einasto fitting formulae in the one-halo term of the model.

### 3.2 The two-halo term

The two-halo term of the model is specified by the bias factor, $b(M)$, and the mass autocorrelation function calculated from linear theory, $\xi_{\rm lin}(r)$. Halo bias has been studied extensively in the context of hierarchical structure formation scenarios. Assuming a Gaussian distribution of initial density fluctuations specified by $\sigma(M)$, the *rms* linear mass fluctuation (extrapolated to $z = 0$) within spheres that on average contain mass $M$, Mo and White (1996) derive an analytic model for halo bias, $b(\nu, z)$, where

$$\nu = \left[\frac{\delta_c(z)}{\sigma(M)}\right] \qquad (13)$$

is the dimensionless amplitude of fluctuations, or peak height, that produces halos of mass $M$ at redshift $z$ and $\delta_c(z)$ is the linear overdensity (again extrapolated to $z = 0$) for which a spherical perturbation would collapse at redshift $z$.. The characteristic halo mass for clustering $M_*(z)$ is defined by $\sigma(M_*) = \delta_c(z)$ and halos more (less) massive than $M_*$ are more (less) strongly clustered than the underlying mass density field. For the Millennium Simulation cosmology, $M_*(z = 0) = 6.15\times10^{12}\ h^{-1}M_\odot$.

Mo and White (1996) showed that their model accurately describes the bias in the autocorrelation function of dark matter halos with respect to the that of the mass in cosmological N-body simulations. Further testing against higher resolution simulations has led to modifications and improvements in the model (Jing 1998; Governato et al. 1999; Sheth and Tormen 1999; Kravtsov and Klypin 1999; Colberg et al. 2000; Sheth et al. 2001; Seljak and Warren 2004; Mandelbaum et al. 2005). Most recently, Gao et al. (2005) compared these models with halo bias in the Millennium Run. Figure 1 of Gao et al. (2005) shows that the Millennium Run results are reasonably well-matched by the bias model of Sheth and Tormen (1999)

$$b(\nu) = 1 + \frac{a\nu^2 - 1}{\delta_c} + \frac{2p}{\delta_c(1 + (a\nu^2)^p)}, \qquad (14)$$

with the parameter values $a = 0.73$ and $p = 0.15$ of Mandelbaum et al. (2005) based on fits to the simulations of Seljak and Warren (2004). We therefore adopt eq. 14 with these parameter values as the bias formula in the two-halo term of our model for $\xi_{\rm hm}$.

### 3.3 Model fitting results

Figure 2 shows the accuracy of our model when we choose the halo density profile to be of NFW form. The downward pointing arrows indicate the transition scale $r_{\rm trans}$ between the one-halo and two-halo regimes of the model, also listed in Table 1. We take the halo mass in the model to be the geometric mean of the upper and lower halo mass limits in each halo sample, i.e., $M_{\rm model} = (M_{\rm lo}M_{\rm hi})^{1/2}$. Here we take the concentration to be a free parameter and compare our best fit values to the concentration-mass relations proposed by various authors. The best fit value is obtained by minimizing the root mean square of $(\xi_{\rm hm} - \xi_{\rm model})/\xi_{\rm hm}$.

Several trends are apparent in the accuracy of our model fits. In the one-halo regime, the NFW profile fits the halo density profile to within about 10%. There is some indication of the systematic "U-shaped" residuals found by N04 for fits to individual halo density profiles with the NFW formula. This indicates that the shape of the NFW profile does not perfectly capture the simulation results. We return to this issue later, when we examine the accuracy of fits using eq. 10 to model the halo density profile.

In the two-halo regime, the deviations in the model at large separations, $r \gtrsim 3\ h^{-1}$Mpc, are dominated by the quasi-linear distortion due to the large-scale movement of halos with respect to each other. This is illustrated by the solid line in Figure 2 which shows the ratio of the mass autocorrelation function to the linear theory prediction, $\xi_{\rm mm}/\xi_{\rm lin}$. This distortion has been investigated in numerous studies of the matter power spectrum (Seljak 2000; Ma and Fry 2000; Scoccimarro et al. 2001; Smith et al. 2003; Cole et al. 2005) and various correction factors have been proposed. In this work we prefer to neglect the distortion and adopt the simpler assumption of pure linear theory (Peacock and Smith 2000). This approach simplifies the calculation of the model and avoids the introduction of the additional parameters that are present in correction factors proposed by Smith et al. (2003) and Cole et al. (2005) at the cost

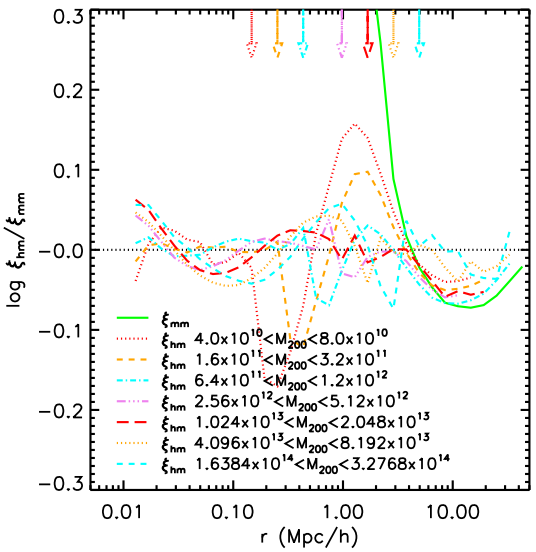


**Figure 2.** Deviations between our measured halo-mass cross-correlations and the simple model given by eqs. 5-7 assuming the NFW profile in the one-halo term. On large scales, $r \gtrsim 3\ h^{-1}$Mpc, the deviations are dominated by a quasi-linear distortion that is apparent in the ratio of the mass autocorrelation function to the linear theory prediction, $\xi_{\rm mm}/\xi_{\rm lin}$ (solid line). For low mass halos, $M_{200} \lesssim 3.2\times10^{11}$, the model also fails on intermediate scales suggesting a cut-off in power should be applied to the linear prediction on these scales. Otherwise the accuracy of the model better than $\simeq 10\%$.

of a systematic residual in our model fits on the order of 25% at $\sim 10\ h^{-1}$Mpc.

In the two lowest mass halo samples shown in Figure 2, the two-halo term in the model appears to overpredict $\xi_{\rm hm}$ at overdensities corresponding to $\xi_{\rm hm} \gtrsim 7$. This suggests that the linear theory prediction should also be modified by a cutoff in power at small scales, as suggested by Smith et al. (2003). We investigate this in further detail in Figure 3, where we examine the linear and quasi-linear terms predicted by the Smith et al. (2003) HALOFIT model for the Millennium Simulation cosmology. The correlation function is related to the power spectrum by the integral relation

$$\xi(r) = \int \Delta^2(k) \frac{\sin kr}{kr} \frac{dk}{k}, \qquad (15)$$

and the HALOFIT model power spectrum is given by the sum of the quasi-linear and one-halo terms,

$$\Delta^2(k) = \Delta^2_{\rm Q}(k) + \Delta^2_{\rm H}(k), \qquad (16)$$

where the quasi-linear term $\Delta^2_{\rm Q}(k)$ includes an exponential cutoff at the nonlinear wavenumber $k_\sigma \simeq 0.3\ h$ Mpc$^{-1}$ for $\Lambda$CDM .

The top panel of Figure 3 shows that the correlation function calculated from the HALOFIT model power spectrum provides a good fit to the mass autocorrelation function $\xi_{\rm mm}$. The cutoff in power at high $k$ built into the HALOFIT model corresponds to a flattening of the corresponding correlation function, $\xi_{\rm Q}$ with respect to the linear theory prediction, $\xi_{\rm lin}$ at an overdensity $\xi_{\rm Q} \simeq 4$. Smith et al. (2003) provide fitting formulae for $\Delta^2_{\rm Q}(k)$ and $\Delta^2_{\rm H}(k)$, each with numerous parameters tuned to give a good match to the matter power spectrum in various CDM-based cosmological N-body simulations. However, Figure 3 shows that $\xi_{\rm Q}$ cannot be used to improve the model for $\xi_{\rm hm}$ of low-mass halos. This is illustrated in the bottom panel, where we show the ratios $\xi_{\rm hm}/\xi_{\rm Q}$ and $\xi_{\rm hm}/\xi_{\rm lin}$ for halos with mass $4.0\times10^{10}\ h^{-1}M_\odot < M_{200} < 8.0\times10^{10}\ h^{-1}M_\odot$. We find that using the quasi-linear term from the HALOFIT model actually produces a marginally poorer fit to the measured shape of halo-mass cross-correlations. The HALOFIT model imposes a cutoff in power at the non-linear wavenumber $k_\sigma$. Our results suggest that the Smith et al. (2003) prescription adopts a value of $k_\sigma$ that is too low in the present context. Modifying their prescription for the non-linear scale would require the recalibration of all of the fitting formulae in the HALOFIT model in order to recover the fit to the mass autocorrelation function. This is beyond the scope of the present paper.

### 3.4 Halo concentrations

Figure 4 shows the best-fit NFW concentration parameter values versus halo mass for our model fits. Also shown are the predictions of the concentration-mass models proposed by Eke et al. (2001, hereafter ENS), Bullock et al. (2001, hereafter B01), and the power-law fits of Macciò et al. (2007, hereafter M07) and Neto et al. (2007). Our best-fit values appear to follow the B01 and M07 results for halo masses $M_{\rm vir} \lesssim 5\times10^{12}$, but at higher masses the results are better described by the ENS model. We find that a power-law provides a reasonable fit to the data, with the same normalization, but a slightly shallower slope ($c \propto M^{-0.080}$) than found by M07 and Neto et al. (2007) ($c \propto M^{-0.109}$). We note that the difference between all these models is relatively small with respect to the $1-\sigma$ scatter, $\Delta \log(c_{\rm vir}) = 0.14$, found for individual halos in B01. Since the ENS model provides a reasonably close match to our best-fit concentration values and has been calibrated for redshifts $z > 0$ and for different cosmologies, we adopt it as our halo concentration model hereafter.

### 3.5 Halo density profile

In this subsection we investigate whether our model is improved if we change the choice of halo density profile. We here use the Einasto profile (eq. 10), the improved fitting formula proposed by N04. This contains an additional shape parameter, $\alpha$, which controls the rate at which the slope of the density profile changes with radius, with typical values lying in the range $[0.12, 0.22]$ (N04, Prada et al. 2006).

Figure 5 shows the deviations of the measured halo-mass cross-correlations from our best fits using the Einasto formula. Here we focus on halo samples with $M_{200} > 6.4\times10^{11}\ \ h^{-1}M_\odot$, since deviations from the fits are then not dominated by the inadequacy of the two-halo term on intermediate scales (see Section 3.3).

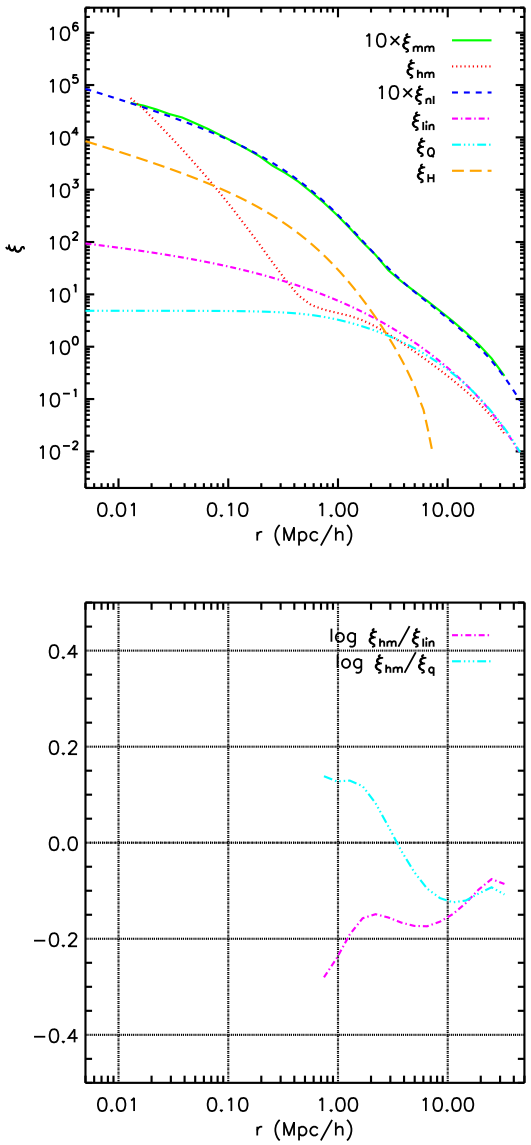


**Figure 3.** *Top panel:* Mass autocorrelation function, $\xi_{\rm mm}$, and halo-mass cross-correlation functions, $\xi_{\rm hm}$, for low-mass halos ($4.0 \times 10^{10} < M_{200} < 8.0 \times 10^{10}$). Also shown are the predictions of linear theory $\xi_{\rm lin}$ and of the Smith et al. (2003) HALOFIT model. Neither $\xi_{\rm lin}$ nor the HALOFIT quasilinear model $\xi_{\rm Q}$ provide a good match to the shape of $\xi_{\rm hm}$ on large scales. *Bottom panel:* The ratio between $\xi_{\rm hm}$ and the linear and quasilinear predictions shows that the *shape* of $\xi_{\rm hm}$ is marginally better fit by $\xi_{\rm lin}$ than by $\xi_{\rm Q}$.

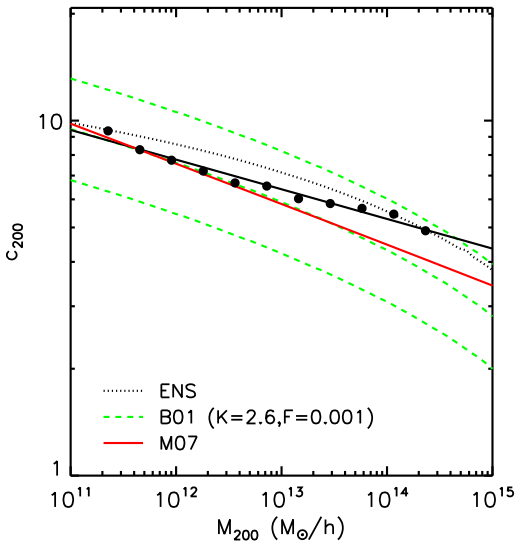


**Figure 4.** NFW concentration versus halo mass from $\xi_{\rm hm}$ model fits compared with the predictions of various models. The solid line shows the best-fit power law with $c \propto M^{-0.080}$.

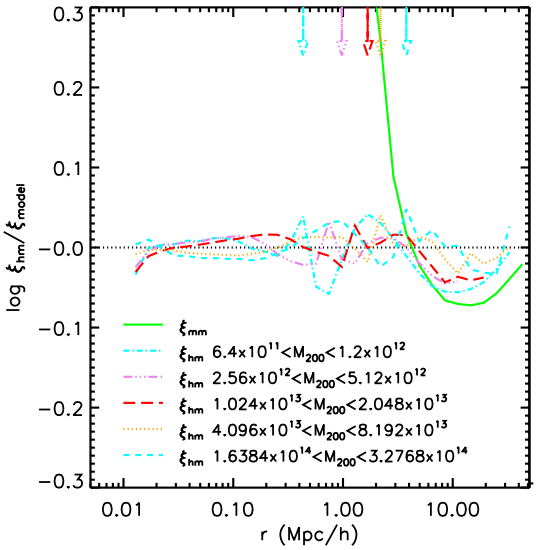


**Figure 5.** Deviations between our measured halo-mass cross-correlations and the simple model given by eqs. 5-7 with the Einasto profile in the one-halo term. On small scales the Einasto profile provides a better fit than the NFW profile, with deviations $\lesssim 5\%$.

The deviations are reduced significantly by using the Einasto model, $\lesssim 5\%$ compared to $\lesssim 10\%$ for fits using the NFW profile. The best-fit values of $\alpha$ are shown as a function of halo mass in Figure 6. We find that $\alpha$ tends to increase with halo mass, ranging from $\alpha \simeq 0.12$ for $M_{200} \simeq 10^{12}\ \ h^{-1}M_{\odot}$ to $\alpha \simeq 0.2$ for $M_{200} \simeq 3 \times 10^{14}\ \ h^{-1}M_{\odot}$.

### 3.6 Higher redshift results

Since galaxy-galaxy lensing studies are sensitive to lenses at redshifts well above zero, it is interesting to check our models against cross-correlations at $z > 0$. In the COSMOS survey, for example, the galaxy-galaxy lensing signal is significant for lenses over the redshift range $0.2 < z < 1.2$ with the main contribution from $z \simeq 0.5 - 0.9$ (A. Leauthaud, private communication).

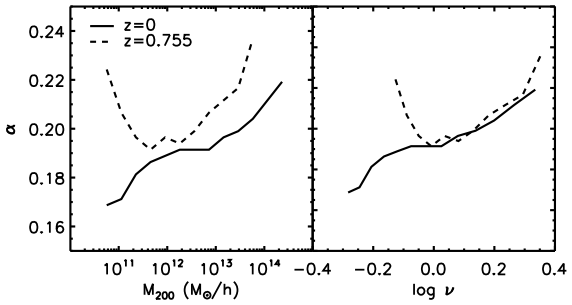


**Figure 6.** Best-fit value of $\alpha$ from the Einasto fitting formula versus halo mass. Higher values of $\alpha$ correspond to density profiles that becomes shallower more quickly towards halo centre. The best-fit value of $\alpha$ tends to increase with halo mass.

Figure 7 shows $\xi_{\rm hm}$ for the $z = 0.755$ output of the Millennium Simulation. The results are qualitatively similar to those at $z = 0$, and the bottom panel of the figure shows the deviations from the best fits using our (Einasto) model. We find that the deviations are on the order $\pm 10\%$ for the higher redshift $\xi_{\rm hm}$. Figure 6 also shows the best fit values of $\alpha$ for this redshift. As in the $z = 0$ case, we find that $\alpha$ tends to increase with mass for $M_{200} \gtrsim 3 \times 10^{11}\ \ h^{-1}M_{\odot}$. In the left panel of this figure we plot the best fit $\alpha$ values against the peak height defined by eq. 13. Plotted in this way, we find that the $z = 0$ and $z = 0.755$ results are in good agreement with each other. We note that a similar result has been obtained by Gao et al (in preparation) in a study of cluster halos from the Millennium Simulation. This provides a simple way to estimate appropriate $\alpha$ values for other redshifts and masses.

### 3.7 Shear

Galaxy-galaxy lensing studies measure the average tangential distortion or shear of background source galaxies due to foreground lenses. If the redshift distributions of the sources and lenses are known, the average tangential shear, $\gamma_t$, is related to the surface mass density as follows

$$\Sigma_{\rm crit}\gamma_t = \overline{\Sigma}(< R) - \Sigma(R) \equiv \Delta\Sigma(R), \qquad (17)$$

where $\overline{\Sigma}(< R)$ is the mean surface density within the projected radius $R$, and the critical surface density is given by

$$\Sigma_{\rm crit} = \frac{c^2}{4\pi G}\frac{D_s}{D_l D_{ls}}, \qquad (18)$$

where $D_s$ and $D_l$ are the angular diameter distances to the lens and the source, respectively, and $D_{ls}$ is the angular diameter distance between the lens and the source. In order to compare our results with observational measurements, we calculate the surface mass density by projecting the three-dimensional mass density:

$$\Sigma(R) = 2\int_r^{\infty} \frac{\Delta\rho(r)}{\sqrt{r^2 - R^2}} r{\rm d}r, \qquad (19)$$

where $\Delta\rho(r) \equiv \rho(r) - \overline{\rho}$.

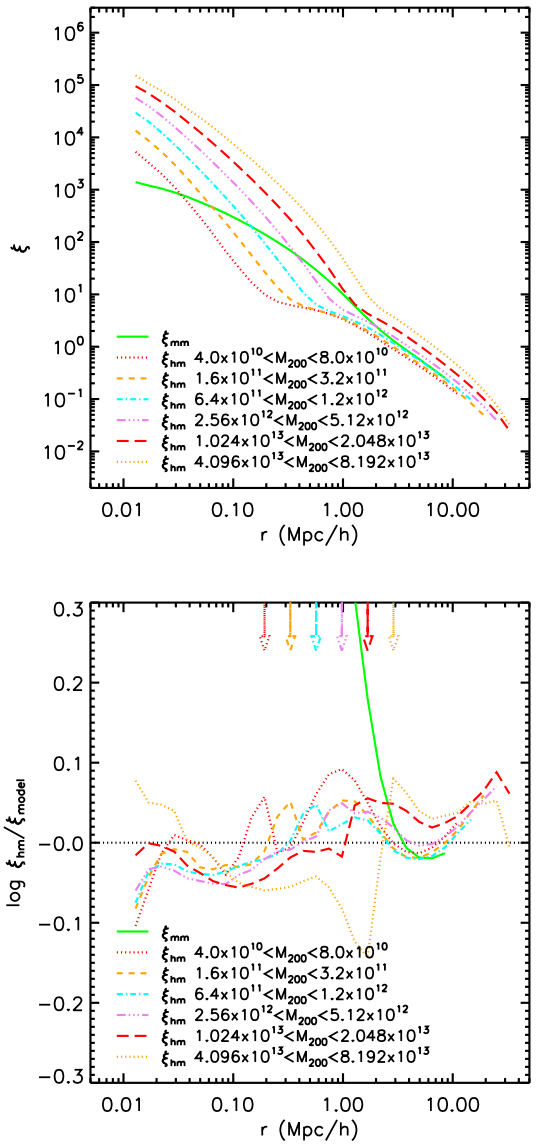


**Figure 7.** *Top panel:* Halo-mass cross-correlations calculated at $z = 0.755$. *Bottom panel:* Deviations between $\xi_{\rm hm}$ and our model assuming the ENS halo concentration relation and the Einasto density profile. Deviations from the model are on the order of $10 - 20\%$.

Figure 8 shows the quantity $\Delta\Sigma(R)$ calculated from our $\xi_{\rm hm}$ curves and our model fits. Note that the model fits have not been recalculated to minimize the deviations in $\Delta\Sigma(R)$. We find that down to a scale of $\simeq 0.03 - 0.05\ \ h^{-1}$Mpc, below which our calculation of $\overline{\Sigma}(R)$ from the simulation becomes unreliable, the deviations from the model fits are $\lesssim 10\%$ for both $z = 0$ and $z = 0.755$.

## 4 GALAXY-MASS CROSS-CORRELATIONS

We now investigate cross-correlations between galaxies and mass in the Millennium Simulation. As described

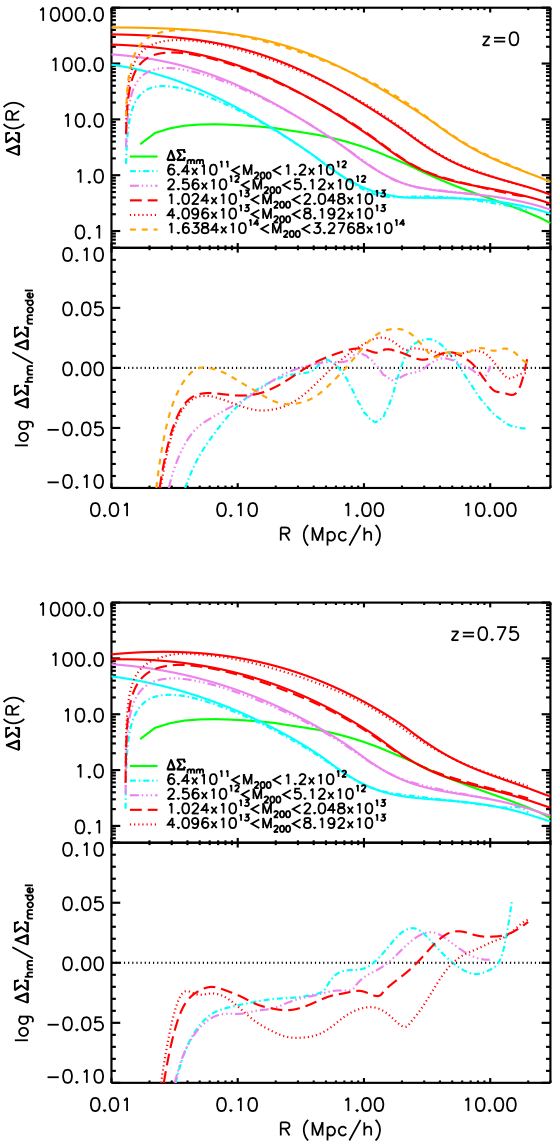


**Figure 8.** *Top panels:* $\Delta\Sigma(R)$ calculated from $\xi_{\rm hm}$ at $z = 0$ and $z = 0.755$. Solid lines show $\Delta\Sigma(R)$ corresponding to best fits to $\xi_{\rm hm}$. *Bottom panels:* Deviations from our fits. The downturn at small scales $r \lesssim 0.03\ h^{-1}$Mpc is due to integrating over scales below the resolution limit of the simulation. On scales larger than this, the magnitude of the deviations are on the order of 10% in terms of $\Delta\Sigma(R)$.

in Section 2, semi-analytic models have been grafted onto the simulation in order to predict the evolution of the galaxy population. A central galaxy is associated with the main subhalo of each FoF halo and satellite galaxies are associated with the other subhalos. In addition, there are so-called 'orphan' galaxies. These are satellite galaxies whose associated subhalos have been tidally stripped to below the resolution limit of the simulation. Such a galaxy remains identified with the individual particle which was the most bound member of the subhalo at the last time it could be identified. Orphan galaxies are assumed to survive for an estimated dynamical friction time, after which they merge with the central galaxy of their halo. They are a significant fraction of the faint galaxies in the model. Gao et al. (2004), Wang et al. (2006) and Sales et al. (2007) show that they must be included if the model is to predict the small-scale clustering of galaxies accurately.

### 4.1 Cross-correlations between central galaxies and mass

We first consider cross-correlations between central galaxies and mass. Since central galaxies are placed on the most bound particle of their host halos, $\xi_{\rm gm}$ for central galaxies is equivalent to $\xi_{\rm hm}$ averaged over the corresponding sample of FoF halos, and so should be similar to the $\xi_{\rm hm}$ presented in Section 3 provided that central galaxies are selected according to a property that correlates well with host halo mass. Figure 9 shows $\xi_{\rm gm}$ for central galaxies selected according to r-band absolute magnitude in the range $-20 < M_r < -24$. These cross-correlations indeed appear very similar in shape to those of Figure 1.

We apply the simple model presented in Section 3 based on the Einasto profile of eq. 10. We take the mass of the host halo as a free parameter which determines the bias factor according to eq. 14 and the radius and concentration of the mean halo density profile according to the ENS model. The best fit value of the halo density profile parameter $\alpha \simeq 0.15$ for the central galaxy $\xi_{\rm gm}$. This is quite similar to the values found above for halos in the relevant mass ranges.

The distribution of host halo masses for central galaxies in the luminosity range $-21 < M_r < -20$ is shown in Figure 10. This distribution is highly asymmetric and ranges over four orders of magnitude in mass. Nevertheless, the best fit model recovers the mean halo mass within about 30%. The bottom panel of the figure shows mean and best-fit halo mass values as a function of $M_r$. The fit values tend to underestimate the mean halo mass, typically by about 30%.

### 4.2 Cross-correlations between satellite galaxies and mass

We now consider cross-correlations between satellite galaxies and the mass. These galaxies were once associated with the dominant subhalo of a FoF group but are now centred on a secondary subhalo within a larger FoF group and may have experienced significant mass loss due to tidal stripping. Indeed, as noted above, a significant fraction are 'orphans' and have lost their subhalo entirely, remaining associated with the particle which lay at subhalo centre when it was last identified. Observation shows that the baryonic components of galaxies are substantially overdense with respect to the dark matter, and simulations suggest that they are therefore more resistant to tidal disruption (Katz et al. 1992, 1996). The semi-analytic galaxy formation model takes this into account by allowing orphans to survive for a dynamical friction time before merging them with the central galaxies of their halos.

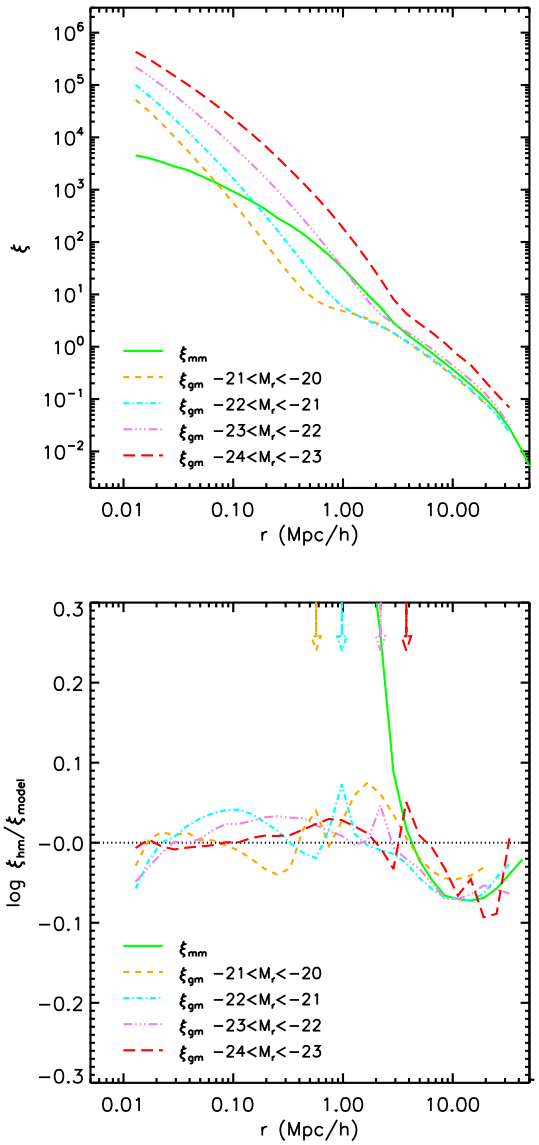


**Figure 9.** *Top panel:* Galaxy-mass cross-correlations at $z = 0$ for central galaxy samples selected according to r-band absolute magnitude. *Bottom panel:* Deviations from our model for halo-mass cross-correlations, where the mean host halo mass has been taken as a free parameter.

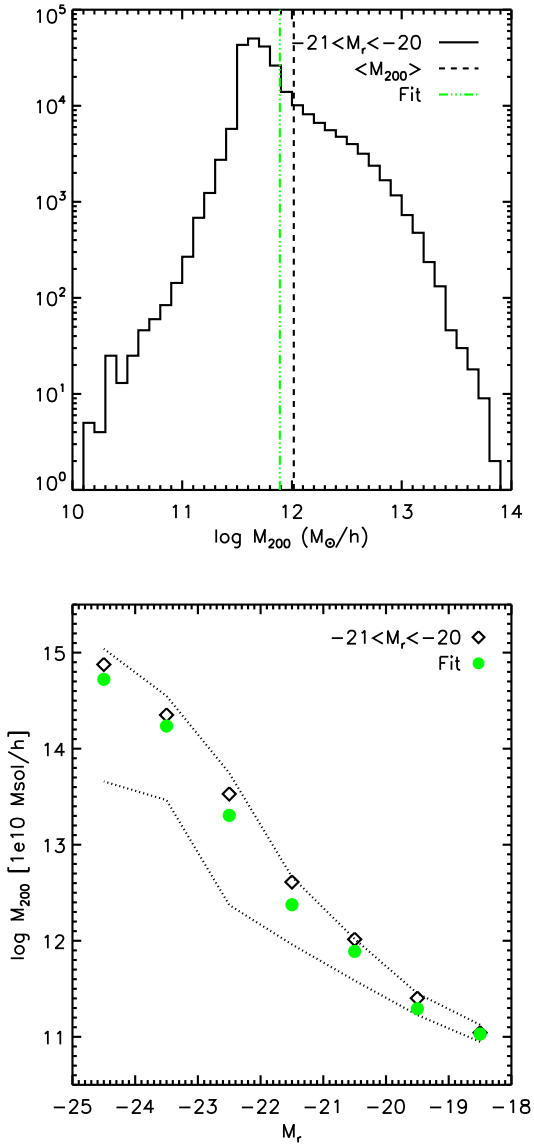


**Figure 10.** *Top panel:* Distribution of host halo mass $M_{200}$ for central galaxies with $-21 < M_r < -20$. *Bottom panel:* Mean host halo $M_{200}$ (open diamonds) with 20-and 80-percentile values (dotted lines) are compared with the best-fit values recovered by modelling galaxy-mass cross-correlations (solid circles).

Table 2 shows the numbers of central and satellite galaxies in the Millennium Simulation model of Croton et al. (2006) as a function of $M_r$. Although there are fewer satellites than central galaxies for all $M_r \leq -17$, the fraction of satellites increases with decreasing luminosity, and is about 40% of the galaxy population for $-19 < M_r < -17$. The fraction of orphans also increases with decreasing luminosity, and is more than half of the total satellite population in the $-18 < M_r < -17$ magnitude range.

Figure 11 shows $\xi_{\rm gm}$ for "subhalo satellites", i.e., satellite galaxies hosted by intact subhalos (top panel) and for orphan satellites (bottom panel). For both types of satellite, the cross-correlation function is positively biased with respect to $\xi_{\rm mm}$ on large scales, $r \gtrsim 1\ h^{-1}$Mpc. This reflects the fact that relatively bright satellite galaxies almost all reside in halos more massive than $M_*$, the characteristic mass at which halos are as strongly clustered as the underlying mass density field.

On small scales, $r \lesssim 0.1\ h^{-1}$Mpc, the shape of $\xi_{\rm gm}$ for satellite subhalos reflects the mass associated with the individual subhalos. A comparison between the $\xi_{\rm gm}$ curves in the top panel of Figure 11 and those in Figure 9 shows that the average density profile of a satellite galaxy with a given luminosity is quite similar in both shape and amplitude to that of a central galaxy with the same luminosity. In detail, the subhalo satellite $\xi_{\rm gm}$ is

**Table 2.** Galaxy properties.

| $M_r$ | $N_{\rm central}$ | $< M_{200} >_{\rm central}$ $[\,h^{-1}M_\odot]$ | $N_{\rm subhalo}$ | $N_{\rm orphan}$ | $f_{\rm sat}$ | $< M_{200} >_{\rm host}$ $[\,h^{-1}M_\odot]$ | $r_{\rm subhalo}$ $[\,h^{-1}{\rm Mpc}]$ | $r_{\rm orphan}$ $[\,h^{-1}{\rm Mpc}]$ |
|---|---|---|---|---|---|---|---|---|
| $[-17,-18]$ | 1927798 | $4.5\times10^{10}$ | 602965 | 752317 | 0.41 | $6.6\times10^{13}$ | 0.52 | 0.36 |
| $[-18,-19]$ | 1252316 | $1.1\times10^{11}$ | 473054 | 404325 | 0.41 | $6.9\times10^{13}$ | 0.55 | 0.32 |
| $[-19,-20]$ | 923701 | $2.0\times10^{11}$ | 308907 | 209794 | 0.35 | $7.7\times10^{13}$ | 0.59 | 0.29 |
| $[-20,-21]$ | 600710 | $7.8\times10^{11}$ | 165187 | 67691 | 0.27 | $8.5\times10^{13}$ | 0.66 | 0.26 |
| $[-21,-22]$ | 236524 | $2.4\times10^{12}$ | 35953 | 7988 | 0.15 | $1.0\times10^{14}$ | 0.83 | 0.23 |
| $[-22,-23]$ | 15984 | $2.0\times10^{13}$ | 1553 | 372 | 0.10 | $2.3\times10^{14}$ | 1.35 | 0.17 |
| $[-23,-24]$ | 617 | $1.7\times10^{14}$ | 27 | 3 | 0.04 | $4.7\times10^{14}$ | 2.42 | 0.33 |
| $[-24,-25]$ | 12 | $5.3\times10^{14}$ | 0 | 0 | 0 | 0 | 0 | 0 |

denser by $\simeq 10-20\%$ with respect to the corresponding central galaxy $\xi_{\rm gm}$, reflecting the higher concentration of subhalos compared to main halos (Bullock et al. 2001).

In the case of orphan satellites, negligible mass is associated with the satellite itself. On small scales the shape of the cross-correlation function reflects that of the host halos after convolution with the mean radial distribution of orphans within their hosts. Since orphans are created by tidal stripping, they are found predominantly close to the centres of their hosts where tidal forces are strongest. Their radial profile is therefore highly centrally concentrated (Gao et al. 2004). Table 2 shows that the mean distance of orphan satellites from the centres of their hosts is significantly smaller than that of subhalo satellites. As a result, the orphan satellite $\xi_{\rm gm}$ is overdense on small scales with respect to $\xi_{\rm mm}$, since the one-halo term of the latter reflects the halo density profile convolved with itself (Ma and Fry 2000).

The cross-correlation with mass for *all* satellite galaxies is shown in Figure 12. This is simply a linear combination of $\xi_{\rm gm}$ for the subhalo and orphan satellites, weighted by the relative fractions of each type. The shape of the resulting function appears quite simple: unlike $\xi_{\rm gm}$ for the subhalo satellites, $\xi_{\rm gm}$ for the total satellite sample is positively biased with respect to $\xi_{\rm mm}$ on all scales, even for faint galaxy samples. In fact, its shape follows that of $\xi_{\rm mm}$ quite closely, with the addition of an upturn on small scales due to the mass associated with the individual subhalos. Encouraged by this, we propose the following model for cross-correlations between satellite galaxies and the mass:

$$\xi_{\rm gm,sat}(r) = \frac{\rho_{\rm halo}(r;c,M)}{\overline{\rho}_{\rm m}} + b(M_{\rm host})\xi_{\rm mm}(r)\left[1+\beta\exp\left(-\frac{r}{r_\beta}\right)\right]. \quad (20)$$

On scales $r \gg r_\beta$, $\xi_{\rm sat}$ is equal to the product of the mass autocorrelation function and the bias factor $b(M_{\rm host})$, where $M_{\rm host}$ is the average mass of halos which host satellite galaxies of a given luminosity. On scales $r \lesssim 2\ h^{-1}$Mpc, a scale-dependent bias is apparent in the satellite $\xi_{\rm gm}$, which we attempt to model with an exponential function. In eq. 20, the parameters $r_\beta$ and $\beta$ control the characteristic scale and amplitude of this scale-dependent bias. On small scales, $r \lesssim 0.1\ h^{-1}$Mpc, the satellite model is dominated by the first term due to the subhalo density profile.

Figure 12 shows the deviations of this model from the satellite $\xi_{\rm gm}$ measured in the simulation. Since a nonlinear model for $\xi_{\rm mm}$ is used as the basis of the satellite model on large scales, the systematic residuals in the fits to the halo and central galaxy cross-correlation functions are not present in the satellite model fits. The main deficiency in the satellite model is in reproducing the scale-dependent bias. The fits shown in Figure 12 were obtained using single values of $r_\beta = 2\ h^{-1}$Mpc and $\beta = 0.5$. They could be improved somewhat by varying these values for the different satellite galaxy luminosity bins, but systematic residuals still remain because the exponential function is only a crude match to the shape of the scale-dependent bias.

The distribution of host halo masses for satellite galaxies in the luminosity range $-21 < M_r < -20$ is shown in Figure 13. The distribution spans five orders of magnitude in mass. Nevertheless, the best-fit model recovers the mean halo mass to within about 30%. The bottom panel shows mean and best-fit halo mass values as a function of $M_r$. The values obtained from fitting the cross-correlations are accurate for host halo masses in the range $-22 < M_r < -19$, but can differ from the true values by as much as 50% for host halos outside this intermediate range.

The model parameters entering the first term in eq. 20 are the concentration, $c$, and the mass, $M_{200}$, of the halo density profile fitting formula. However, the best fitting parameter values (shown in Figure 13; the concentration is taken as the typical value for halos of each mass) are not easily interpreted.

### 4.3 Cross-correlations with mass for all galaxies

In Figure 14 we present cross-correlations of all galaxies with mass. This is simply the linear combination of the cross-correlations for central and satellite galaxies, weighted by the relative fractions of each type, i.e.:

$$\xi_{\rm gm,all} = (1-f_{\rm sat})\xi_{\rm gm,central} + f_{\rm sat}\xi_{\rm gm,sat}, \quad (21)$$

where the fraction of satellite galaxies is defined as $f_{\rm sat} = N_{\rm sat}/(N_{\rm central}+N_{\rm sat})$. The satellite fraction in each luminosity range strongly affects the shape of $\xi_{\rm gm}$ for galaxies of that luminosity. Table 2 shows that $f_{\rm sat}$ ranges from $\simeq 40\%$ in the lowest luminosity bins, $M_r > -19$, to $\simeq 5\%$ for $M_r < -22$.

Since eq. 21 is a linear combination of two functions

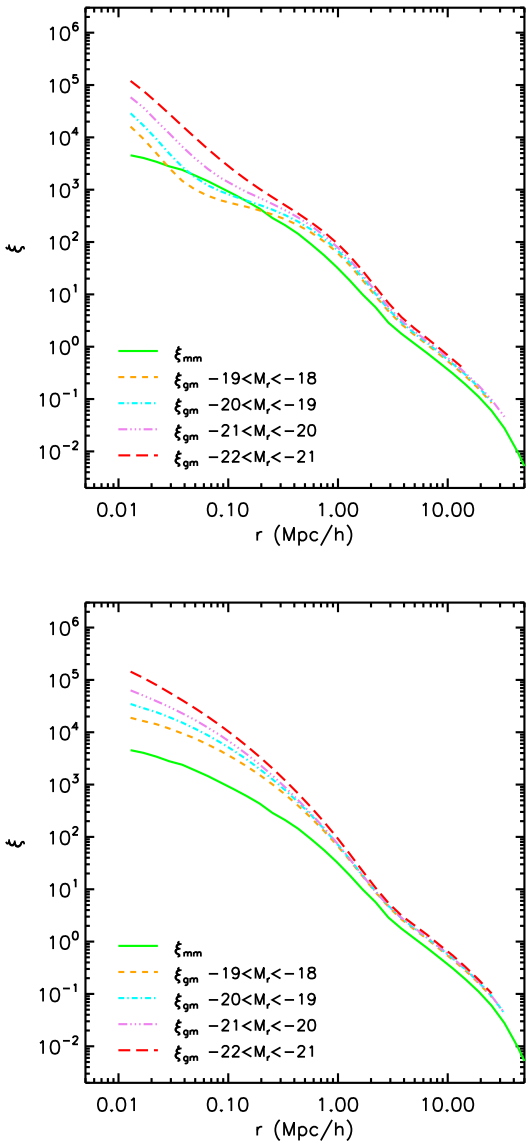


**Figure 11.** Cross-correlation between the mass and satellite galaxies with (*top panel*) and without (*bottom panel*) associated subhalos. In both cases, $\xi_{\rm gm}$ is positively biased on large scales, $r \gtrsim 1\ h^{-1}$Mpc indicating that satellites preferentially reside in high mass halos. On small scales $\xi_{\rm gm}$ for subhalo satellites shows an upturn due to the mass bound to the individual subhalos, whereas the orphan satellite $\xi_{\rm gm}$ reflects the density profile of the host halo convolved with the radial distribution of the orphan satellites.

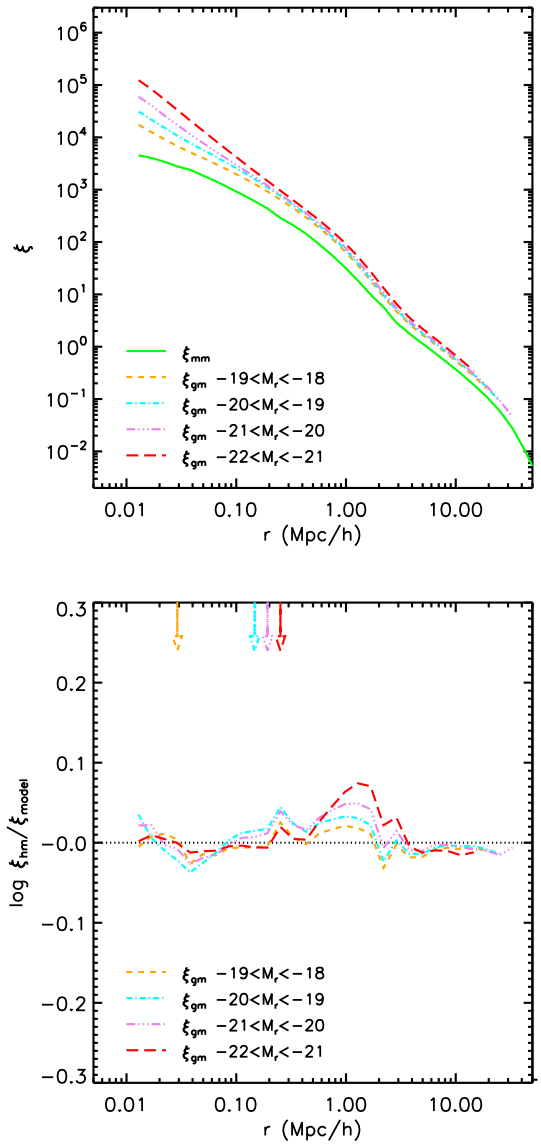


**Figure 12.** *Top panel:* Cross-correlations of the mass with *all* satellite galaxies. In this case the shape of $\xi_{\rm gm}$ is similar to that of $\xi_{\rm mm}$ with an upturn on small scales due to the subhalo mass associated with individual satellites that have not been fully tidally disrupted. *Bottom panel:* Deviations between the satellite $\xi_{\rm gm}$ and the model given by eq. 20. The deviations are largest at intermediate scales, $r \simeq 1\ h^{-1}$Mpc, where the model fails to accurately describe the shape of the scale-dependent bias.

which can differ in value by several orders of magnitude and since $f_{\rm sat}$ is of order unity, $\xi_{\rm gm,all}$ is dominated by the larger of $\xi_{\rm gm,central}$ and $\xi_{\rm gm,sat}$ at most radii. For instance, for $-24 < M_r < -23$, $\xi_{\rm gm,central}/\xi_{\rm gm,sat} \gg 1$ at all radii, thus eq. 21 gives $\xi_{\rm gm,all} \simeq (1 - f_{\rm sat})\xi_{\rm gm,central}$ and the cross-correlation function is very similar to $\xi_{\rm gm,central}$. At lower luminosities, $\xi_{\rm gm,sat}/\xi_{\rm gm,central} \gg 1$ at intermediate radii, $0.1\ h^{-1}{\rm Mpc} < r < 1\ h^{-1}{\rm Mpc}$, so $\xi_{\rm gm,all} \simeq f_{\rm sat}\xi_{\rm gm,sat}$ and in this case the cross-correlation function resembles that of the satellite galaxies.

The combined $\xi_{\rm gm}$ model for central and satellite galaxies contains the following five parameters: $M_{\rm central}, M_{\rm host}, M_{\rm sat}, c_{\rm sat}$, and $f_{\rm sat}$. However, in fitting this composite model to the measured cross-correlations, we obtained best-fit parameter values which were not in good agreement with the true values of $M_{\rm central}, M_{\rm host}$ and $f_{\rm sat}$. This suggests that the shape of $\xi_{\rm gm}$ is degenerate, with various combinations of the five free parameters giving almost equivalent fits.

It is interesting to note that our cross-correlation model is based on components which deviate strongly from power laws, i.e., $\xi_{\rm lin}$, $\xi_{\rm mm}$ and $\rho_{\rm halo}$. Nevertheless,

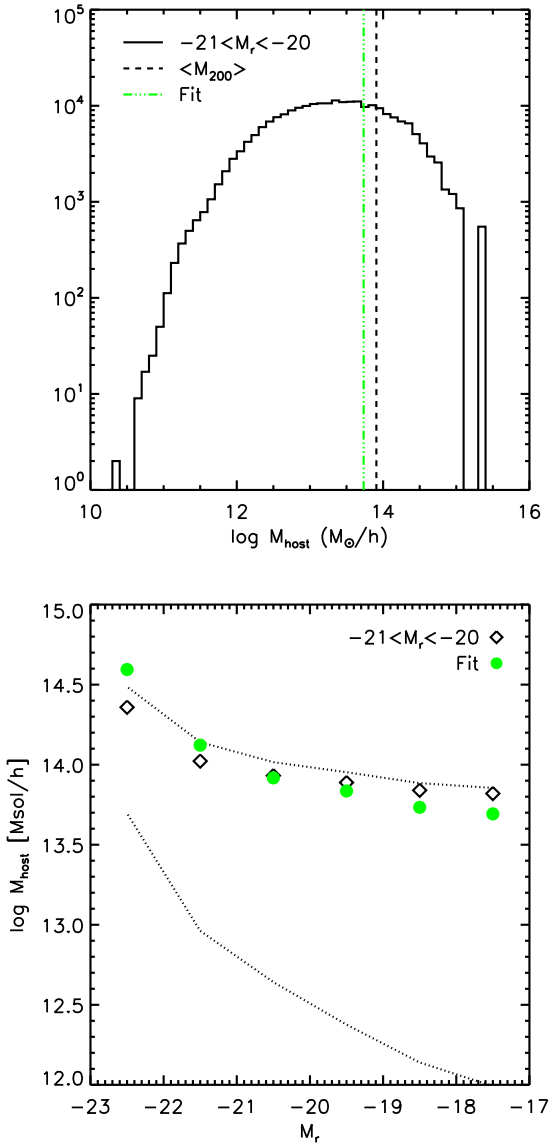


**Figure 13.** *Top panel:* Distribution of host halo $M_{200}$ for satellite galaxies with $-21 < M_r < -20$. *Bottom panel:* Mean host halo $M_{200}$ (open diamonds) with 20-and 80-percentile values (dotted lines) are compared with best-fit values recovered by modelling the satellite-mass cross-correlations (solid circles).

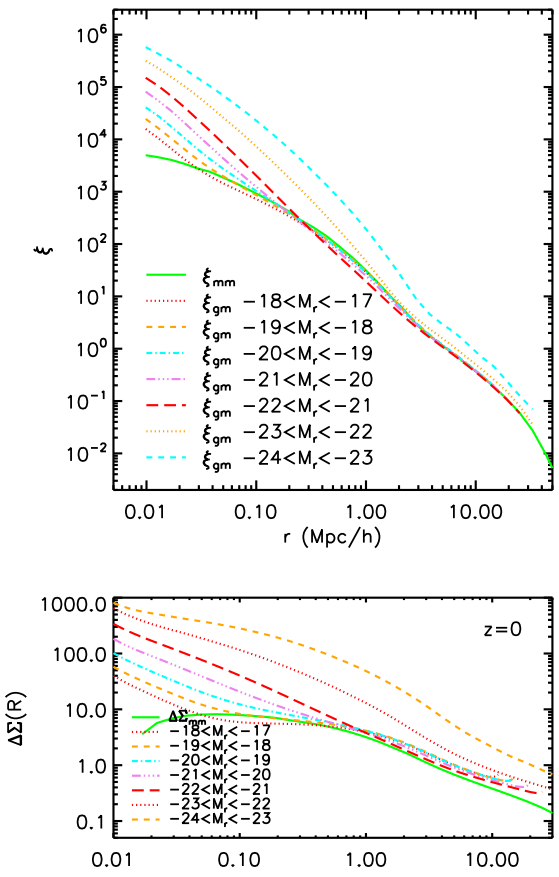


**Figure 14.** *Top panel:* Cross-correlations between all galaxies and the mass at $z = 0$. High-luminosity galaxy samples are dominated by central galaxies, therefore $\xi_{\rm gm}$ resembles our simple model for $\xi_{\rm hm}$. Low-luminosity galaxy samples contain a significant fraction of satellite galaxies and $\xi_{\rm gm}$ follows the shape of $\xi_{\rm mm}$. *Bottom panel:* $\Delta\Sigma(R)$ corresponding to $\xi_{\rm gm}$.

at intermediate luminosities $\xi_{\rm gm,all}$ is reasonably well described by a power-law over a wide range in radius. In order to illustrate this point, we plot in Figure 15 the deviations from power-law fits to $\xi_{\rm gm,all}$. In particular, we find that in the range $-21 < M_r < -20$, $\xi_{\rm gm,all}$ is well fit by a power law with slope $r^{-1.8}$ and the deviations from the fit are $\lesssim 10\%$ at all radii!

For galaxies more luminous than $M_r < -21$, the deviations from best-fit power laws become $\gtrsim 50\%$ at some radii. Galaxies in this luminosity range are dominated by central galaxies, so our model for $\xi_{\rm gm,central}$ can be used to fit observations and provide detailed checks on various aspects of the cosmological and galaxy formation models. At lower luminosities, however, we conclude that some independent information regarding the satellite fraction must be included in order to extract useful information about the average mass of the halos which host satellites. Alternatively, shear data can be stacked around galaxies that are observed to be brighter than all their neighbours, and thus are very likely central galaxies. Our models can be used to predict $\Delta\Sigma(R)$ for direct comparison with such galaxy-galaxy lensing measurements. Examples are shown in the lower panel of Figure 14. It is notable that these curves show a variety of scales and features which should be directly observable.

## 5 SUMMARY

We have calculated cross-correlations between halo centres and the mass, and between galaxies and the mass in the Millennium Simulation of a ΛCDM cosmology. The shape of the halo-mass cross-correlation function

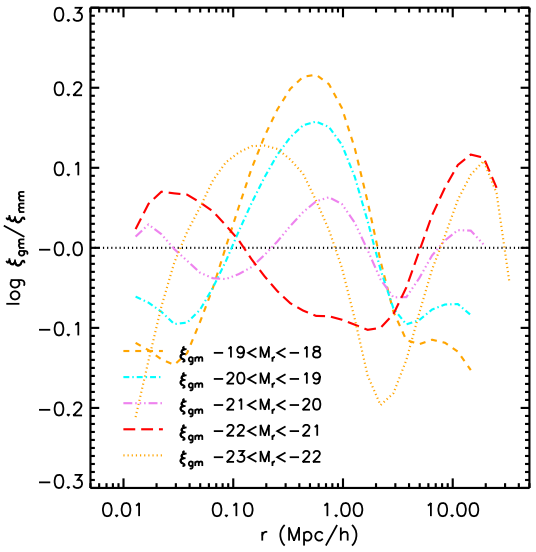


**Figure 15.** Deviations from the best-fitting power laws of our measured cross-correlations between all galaxies and the mass.

$\xi_{\rm hm}$ is well fit by a simple two-part model. On small scales, $\xi_{\rm hm}$ is specified by the halo density profile which is accurately described by the Einasto model advocated by N04. On large scales, $\xi_{\rm hm}$ is specified by the mass autocorrelation function predicted by linear theory and the halo bias model of Sheth and Tormen (1999). The deviations between $\xi_{\rm hm}$ and the best-fit model are dominated by the quasi-linear distortion in $\xi_{\rm mm}$, but are otherwise $\lesssim 5\%$.

The cross-correlation functions of central galaxies, $\xi_{\rm gm,central}$, are reasonably well fit by our model for $\xi_{\rm hm}$. The best-fit models recover the mean halo masses of central galaxies to within 30%. The cross-correlations of satellite galaxies, $\xi_{\rm gm,sat}$ appear qualitatively different from those of halos or central galaxies. Their shape is similar to that of $\xi_{\rm mm}$, with an upturn at small scales due to the mass associated with the individual subhalos in which most satellites reside. A model for $\xi_{\rm gm,sat}$ based on these features reproduces the cross-correlation functions to within 10% and recovers the mean host halo mass to within 50%.

The cross-correlation function of all galaxies, $\xi_{\rm gm,all}$ is simply a linear combination of $\xi_{\rm gm,central}$ and $\xi_{\rm gm,sat}$ weighted by the relative fractions of central and satellite galaxies. For very luminous galaxies, the satellite fraction $f_{\rm sat} \lesssim 10\%$, and $\xi_{\rm gm,all}$ is dominated by the contribution of $\xi_{\rm gm,central}$ . At intermediate luminosities, $-22 < M_r < -20$, $\xi_{\rm gm,all}$ is reasonably well fit by a power law. At lower luminosities the cross-correlation is dominated by the satellite galaxy contribution.

The conversion from the three-dimensional cross-correlations to the directly observable mean tangential shear (which is proportional to $\Delta\Sigma(R)$, the difference between the mean enclosed surface density and the local surface density at each projected radius $R$) accentuates features in the cross-correlations. Galaxy-galaxy lensing surveys typically contain enough information to separate the lenses into likely satellites and likely central systems. As a result, the features seen in our predictions should provide information on cosmological parameters, tidal stripping processes, and the exact way in which galaxies trace the dark matter. If the features are clearly detected where they are expected, this will provide a major challenge to theories which try to replace dark matter by a modification of Einsteinian gravity.

## ACKNOWLEDGMENTS

We thank L. Gao, U. Seljak, N. Padmanabhan, A. Leauthaud, and R. Mandelbaum for useful discussions.

## REFERENCES

Brainerd, T. G., Blandford, R. D., and Smail, I.: 1996, *ApJ* **466**, 623
Bullock, J. S., Kolatt, T. S., Sigad, Y., Somerville, R. S., Kravtsov, A. V., Klypin, A. A., Primack, J. R., and Dekel, A.: 2001, *MNRAS* **321**, 559
Colberg, J. M., White, S. D. M., Yoshida, N., MacFarland, T. J., Jenkins, A., Frenk, C. S., Pearce, F. R., Evrard, A. E., Couchman, H. M. P., Efstathiou, G., Peacock, J. A., Thomas, P. A., and The Virgo Consortium: 2000, *MNRAS* **319**, 209
Cole, S., Percival, W. J., Peacock, J. A., Norberg, P., Baugh, C. M., Frenk, C. S., Baldry, I., Bland-Hawthorn, J., Bridges, T., Cannon, R., Colless, M., Collins, C., Couch, W., Cross, N. J. G., Dalton, G., Eke, V. R., De Propris, R., Driver, S. P., Efstathiou, G., Ellis, R. S., Glazebrook, K., Jackson, C., Jenkins, A., Lahav, O., Lewis, I., Lumsden, S., Maddox, S., Madgwick, D., Peterson, B. A., Sutherland, W., and Taylor, K.: 2005, *MNRAS* **362**, 505
Croton, D. J., Gao, L., and White, S. D. M.: 2007, *MNRAS* **374**, 1303
Croton, D. J., Springel, V., White, S. D. M., De Lucia, G., Frenk, C. S., Gao, L., Jenkins, A., Kauffmann, G., Navarro, J. F., and Yoshida, N.: 2006, *MNRAS* **365**, 11
Davis, M., Efstathiou, G., Frenk, C. S., and White, S. D. M.: 1985, *ApJ* **292**, 371
dell'Antonio, I. P. and Tyson, J. A.: 1996, *ApJ* **473**, L17+
Dubinski, J. and Carlberg, R. G.: 1991, *ApJ* **378**, 496
Einasto, J.: 1965, *Trudy Inst. Astrofiz. Alma-Ata* **51**, 87
Eke, V. R., Navarro, J. F., and Steinmetz, M.: 2001, *ApJ* **554**, 114
Fischer, P., McKay, T. A., Sheldon, E., Connolly, A., Stebbins, A., Frieman, J. A., Jain, B., Joffre, M., Johnston, D., Bernstein, G., Annis, J., Bahcall, N. A., Brinkmann, J., Carr, M. A., Csabai, I., Gunn, J. E., Hennessy, G. S., Hindsley, R. B., Hull, C., Ivezić, Ž., Knapp, G. R., Limmongkol, S., Lupton, R. H., Munn, J. A., Nash, T., Newberg, H. J., Owen, R., Pier, J. R., Rockosi, C. M., Schneider, D. P., Smith, J. A., Stoughton, C., Szalay, A. S., Szokoly, G. P., Thakar, A. R., Vogeley, M. S., Waddell, P., Weinberg, D. H.,

York, D. G., and The SDSS Collaboration: 2000, *AJ* **120**, 1198
Frenk, C. S., White, S. D. M., Efstathiou, G., and Davis, M.: 1985, *Nature* **317**, 595
Gao, L., Springel, V., and White, S. D. M.: 2005, *MNRAS* **363**, L66
Gao, L. and White, S. D. M.: 2007, in preparation
Gao, L. and White, S. D. M.: 2007, *MNRAS* **377**, L5
Gao, L., White, S. D. M., Jenkins, A., Stoehr, F., and Springel, V.: 2004, *MNRAS* **355**, 819
Governato, F., Babul, A., Quinn, T., Tozzi, P., Baugh, C. M., Katz, N., and Lake, G.: 1999, *MNRAS* **307**, 949
Griffiths, R. E., Casertano, S., Im, M., and Ratnatunga, K. U.: 1996, *MNRAS* **282**, 1159
Guzik, J. and Seljak, U.: 2001, *MNRAS* **321**, 439
Guzik, J. and Seljak, U.: 2002, *MNRAS* **335**, 311
Harker, G., Cole, S., Helly, J., Frenk, C., and Jenkins, A.: 2006, *MNRAS* **367**, 1039
Hoekstra, H., Franx, M., Kuijken, K., Carlberg, R. G., and Yee, H. K. C.: 2003, *MNRAS* **340**, 609
Hudson, M. J., Gwyn, S. D. J., Dahle, H., and Kaiser, N.: 1998, *ApJ* **503**, 531
Jing, Y. P.: 1998, *ApJ* **503**, L9+
Katz, N., Hernquist, L., and Weinberg, D. H.: 1992, *ApJ* **399**, L109
Katz, N., Weinberg, D. H., and Hernquist, L.: 1996, *ApJS* **105**, 19
Kravtsov, A. V. and Klypin, A. A.: 1999, *ApJ* **520**, 437
Li, C. et al.: 2006
Ma, C.-P. and Fry, J. N.: 2000, *ApJ* **543**, 503
Macciò, A. V., Dutton, A. A., van den Bosch, F. C., Moore, B., Potter, D., and Stadel, J.: 2007, *MNRAS* **378**, 55
Mandelbaum, R., Tasitsiomi, A., Seljak, U., Kravtsov, A. V., and Wechsler, R. H.: 2005, *MNRAS* **362**, 1451
McKay, T. A. et al.: 2001
Mo, H. J. and White, S. D. M.: 1996, *MNRAS* **282**, 347
Navarro, J. F., Frenk, C. S., and White, S. D. M.: 1996, *ApJ* **462**, 563 (NFW)
Navarro, J. F., Frenk, C. S., and White, S. D. M.: 1997, *ApJ* **490**, 493
Navarro, J. F., Hayashi, E., Power, C., Jenkins, A. R., Frenk, C. S., White, S. D. M., Springel, V., Stadel, J., and Quinn, T. R.: 2004, *MNRAS* **349**, 1039
Neto, A. F., Gao, L., Bett, P., Cole, S., Navarro, J. F., Frenk, C. S., White, S. D. M., Springel, V., and Jenkins, A.: 2007, *ArXiv e-prints* 706
Peacock, J. A. and Smith, R. E.: 2000, *MNRAS* **318**, 1144
Peebles, P. J. E.: 1980, *The large-scale structure of the universe*, Research supported by the National Science Foundation. Princeton, N.J., Princeton University Press, 1980. 435 p.
Prada, F., Klypin, A. A., Simonneau, E., Betancort-Rijo, J., Patiri, S., Gottlöber, S., and Sanchez-Conde, M. A.: 2006, *ApJ* **645**, 1001
Quinn, P. J., Salmon, J. K., and Zurek, W. H.: 1986, *Nature* **322**, 329
Sales, L. V., Navarro, J. F., Abadi, M. G., and Steinmetz, M.: 2007, *MNRAS* **379**, 1475
Scoccimarro, R., Sheth, R. K., Hui, L., and Jain, B.: 2001, *ApJ* **546**, 20
Seljak, U.: 2000, *MNRAS* **318**, 203
Seljak, U. and Warren, M. S.: 2004, *MNRAS* **355**, 129
Seljak, U. and Zaldarriaga, M.: 1996, *ApJ* **469**, 437
Sheldon, E. S., Johnston, D. E., Frieman, J. A., Scranton, R., McKay, T. A., Connolly, A. J., Budavári, T., Zehavi, I., Bahcall, N. A., Brinkmann, J., and Fukugita, M.: 2004, *AJ* **127**, 2544
Sheth, R. K., Mo, H. J., and Tormen, G.: 2001, *MNRAS* **323**, 1
Sheth, R. K. and Tormen, G.: 1999, *MNRAS* **308**, 119
Smith, R. E., Peacock, J. A., Jenkins, A., White, S. D. M., Frenk, C. S., Pearce, F. R., Thomas, P. A., Efstathiou, G., and Couchman, H. M. P.: 2003, *MNRAS* **341**, 1311
Springel, V., Frenk, C. S., and White, S. D. M.: 2006, *Nature* **440**, 1137
Springel, V., White, S. D. M., Jenkins, A., Frenk, C. S., Yoshida, N., Gao, L., Navarro, J., Thacker, R., Croton, D., Helly, J., Peacock, J. A., Cole, S., Thomas, P., Couchman, H., Evrard, A., Colberg, J., and Pearce, F.: 2005, *Nature* **435**, 629
Springel, V., White, S. D. M., Tormen, G., and Kauffmann, G.: 2001a, *MNRAS* **328**, 726
Springel, V., Yoshida, N., and White, S. D. M.: 2001b, *New Astronomy* **6**, 79
Tasitsiomi, A., Kravtsov, A. V., Wechsler, R. H., and Primack, J. R.: 2004, *ApJ* **614**, 533
Wang, L., Li, C., Kauffmann, G., and de Lucia, G.: 2006, *MNRAS* **371**, 537
Weinberg, D. H., Davé, R., Katz, N., and Hernquist, L.: 2004, *ApJ* **601**, 1
White, S.: 1996, in R. Schaeffer, J. Silk, M. Spiro, and J. Zinn-Justin (eds.), *Les Houches Session LX, Cosmology and Large Scale Structure*, IAU Symposium No. 208
Yang, X. H., Mo, H. J., Kauffmann, G., and Chu, Y. Q.: 2003, *MNRAS* **339**, 387